Engineering Applications of Artificial Intelligence 97 (2021) 104009

Contents lists available at ScienceDirect

Engineering Applications of Artificial Intelligence

journal homepage: www.elsevier.com/locate/engappai

# Automation of hemocompatibility analysis using image segmentation and supervised classification

Johanna C. Clauser [a,*], Judith Maas [a], Jutta Arens [a,b], Thomas Schmitz-Rode [a], Ulrich Steinseifer [a,c], Benjamin Berkels [d,e]

[a] Department of Cardiovascular Engineering, Institute of Applied Medical Engineering, Medical Faculty, RWTH Aachen University, Pauwelsstr. 20, 52074 Aachen, Germany

[b] University of Twente Faculty of Engineering Technology, Chair of Organ Support Technologies, Department of Biomechanical Engineering, Drienerlolaan 5, 7522 NB Enschede, Overijssel, NL, The Netherlands

[c] Department of Mechanical and Aerospace Engineering, Faculty of Engineering, Monash Institute of Medical Engineering, Monash University, 17 College Walk, Clayton Victoria 3800, Australia

[d] AICES Graduate School, RWTH Aachen University, Schinkelstr. 2, 52062 Aachen, Germany

[e] Institute for Geometry and Practical Mathematics, RWTH Aachen University, Templergraben 55, 52056 Aachen, Germany

ARTICLE INFO

*Keywords:*
Platelet characterization
Random forest
Segmentation
Standardization
In-vitro test

ABSTRACT

The hemocompatibility of blood-contacting medical devices remains one of the major challenges in biomedical engineering and makes research in the field of new and improved materials inevitable. However, current in-vitro test and analysis methods are still lacking standardization and comparability, which impedes advances in material design. For example, the optical platelet analysis of material in-vitro hemocompatibility tests is carried out manually or semi-manually by each research group individually.

As a step towards standardization, this paper proposes an automation approach for the optical platelet count and analysis. To this end, fluorescence images are segmented using Zach's convexification of the multiphase-phase piecewise constant Mumford–Shah model. The non-background components then need to be classified as platelet or no platelet. For this purpose, a supervised random forest is applied to feature vectors derived from the components using features like area, perimeter and circularity. With an overall high accuracy ($> 93\,\%$) and low error rates ($\leq 5\,\%$), the random forest achieves reliable results. This is supported by high areas under the receiver–operator characteristic curve ($\geq 0.94$) and the prediction–recall curve ($\geq 0.77$), respectively.

We developed a novel method for a fast, user-independent and reproducible analysis of material hemocompatibility tests. The automatized analysis method overcomes the current obstacles in the way of standardized in-vitro material testing and is therefore a unique and powerful tool for advances in biomaterial research.

## 1. Introduction

The biocompatibility of blood contacting medical devices such as artificial heart valves or circulatory support systems remains a major challenge in biomedical engineering. With regard to blood contact, the subtopic of hemocompatibility is of major interest (Ratner, 2007). When a foreign material comes into contact with blood, proteins are immediately adsorbed on the material surface. In the following, the physiological coagulation system is triggered and activated, which finally leads to platelet adhesion and thrombus formation on the surfaces (Jaffer et al., 2015). Possible consequences of such thrombi are failure of the medical device or thromboembolism, which are both highly life-threatening for patients. An anticoagulation therapy can reduce the risk of thrombi; however, it may lead to possible bleeding complications (Ratner et al., 2013). Due to these limitations in the use of artificial blood contacting materials, research and improvements in the field of material hemocompatibility are of great importance.

The hemocompatibility of a material is first evaluated through in-vitro blood tests. A general framework for such tests is defined in the standard DIN ISO 10993-4. However, it consists more of recommendations rather than of clear instructions or regulations (Braune et al., 2016; DIN ISO 10993-4:2017, 2017). For example, the ISO suggests an optical evaluation of adherent platelets after material in-vitro testing by means of different microscopy techniques but does not provide any general instructions as to how the degree of platelet adhesion or activation should be evaluated. Thus, a huge variability of applied test and analysis methods make comparisons between different studies nearly impossible (Braune et al., 2013; Sefton et al., 2001). In the case of microscopy image analysis, adherent platelets are commonly counted

* Corresponding author.
*E-mail address:* clauser@ame.rwth-aachen.de (J.C. Clauser).

https://doi.org/10.1016/j.engappai.2020.104009
Received 16 April 2020; Received in revised form 28 August 2020; Accepted 5 October 2020
Available online xxxx
0952-1976/

manually or semi-manually (Lutter et al., 2015; Pham et al., 2016; Zhou et al., 2008). Besides the lack of transferability of such user-dependent analyses, a (semi-)manual platelet count can be very time consuming and prone to error or subjective interpretation.

Automated image segmentation and classification are beneficial whenever a large amount of data needs to be analyzed. During the last decades, automation and machine learning received increasing attention in biomedical image analysis, e.g. for computed tomography (CT) and magnetic resonance imaging (MRI). While the classical biomedical images present anatomical sections of the body that need to be evaluated with regard to e.g. unphysiological structures or lesions (Sheth et al., 2019; Pereira et al., 2018; Altan and Karasu, 2020), another type of biomedical images depict the patients' blood and displays various types of cells, such as cancer or blood cells (Fuyong et al., 2018; Khan et al., 2020). Generally, the analysis of any biomedical image faces the challenges of individual geometries and uncertain boundaries between objects and requires expert knowledge for the classification of the imaged structures. Especially in the analysis of cells, the variability of a cell type with respect to microscopy technique and quality, patient specificity and the current cell state immensely affect the outcome (Kan, 2017; Akram et al., 2016). Hence, automated cell image analysis in combination with machine learning approaches are scarce and most often require a large database to achieve reliable results (Zinchuk and Grossenbacher-Zinchuk, 2020).

This study presents a new approach to an automatized analysis of fluorescence images for in-vitro hemocompatibility evaluation. For this purpose, we use a piecewise-constant multiphase segmentation algorithm and a supervised random forest.

## 2. Methods

The first part of this chapter contains information about the test setup and the experimental procedure of the in-vitro hemocompatibility study that was carried out for creating a fluorescence image data base. In the second part, mathematical details of the segmentation algorithm are presented. The third part comprises information regarding the supervised random forest, and the last part of this chapter describes a multi-person prediction trial. The entire source code used in this study is available at https://github.com/berkels/platelet-analysis.

### 2.1. Hemocompatibility experiments

The hemocompatibility test series was carried out with three commercial medical grade materials as well as two different in-house produced foils of medical grade polyurethane (see Table 1). Materials were chosen due to comparability to previously conducted studies with these materials (Braune et al., 2017; Clauser et al., 2014; Nadzeyka et al., 2017). The experimental procedure of the static in-vitro experiments is described in detail in Braune et al. (2017). Briefly, duplicates of material samples were incubated for 1 h each with 1 ml of platelet rich plasma (PRP) obtained from fresh human blood (Ethical Committee reference number EK 348/16 and EK 033/18). Afterwards, PRP was removed and material samples were consecutively rinsed with phosphate buffered saline, fixed with 2 % glutaraldehyde (Roth, Germany), rinsed with buffer solution again and finally mounted on microscopy slides (Mowiol, Roth, Germany). Experiments were repeated ten times with different donors.

Microscopy images were acquired with a fluorescence microscope (Axio Observer Z1, Carl Zeiss GmbH, Germany) and a 40-fold magnification (resolution/image: $2752 \times 2208$ px, 24-bit). The images were recorded as $5 \times 5$ tile images with a maximum of 45 tile images distributed across the material sample. For each $5 \times 5$ tile, nine focus points were adjusted manually prior to image recording. Regions of contamination (e.g. mounting medium, air bubbles, glutaraldehyde residues) were excluded from microscopy. Due to a high autofluorescence of PET, light intensity was reduced for this material to 58.32 % compared to the other materials recorded with 100 % light intensity. Following microscopy, the region of interest (ROI) representing the PRP-incubated area was marked on a compilation of all images of one material samples using the software Zen Blue (Carl Zeiss GmbH, Germany). Any image outside the ROI was excluded from the following analysis steps. Additionally, all remaining images underwent a visual inspection, discarding blurred or contaminated (e.g. hair, protein residues) images. In the following, a subset of the remaining images was used for the development of the new analysis method (ground truth), which was afterwards applied to the whole image data set for analyzing the hemocompatibility study.

### 2.2. Image segmentation

The first step in the platelet analysis of an image is to detect all objects shown in that image as a basis to find potential platelets. To simplify this detection, we first removed artifacts and the uneven background illumination from the images using ImageJ (National Institutes of Health, USA). For this, ImageJ's rolling ball algorithm (Ferreira and Rasband, 2012) was applied with a radius of $r = 100$ px, which achieved the best results according to visual verification. Additionally, images were downscaled by the factor 2.777 (final resolution of $991 \times 795$ px, 8-bit) to accelerate the following processing steps. Fig. 1 shows an example image before and after applying the rolling ball algorithm.

As one can see in the background corrected image in Fig. 1, finding potential platelets essentially means separating foreground from background in the image and splitting the foreground into its connected components. This separation is a special image segmentation problem. In general, image segmentation refers to the task of partitioning an image into segments that describe image structures, e.g. foreground and background. More mathematically, it means decomposing an image into disjoint regions that are homogeneous in a suitable sense, e.g. that have a homogeneous color. As one of the fundamental image processing problems, it has been extensively studied in the literature in many contexts and for many applications. For instance, a survey on trends in color image segmentation can be found in Vantaram and Saber (2012). Here, we use the famous Mumford–Shah model to handle the segmentation (Mumford and Shah, 1989).

Mathematically, an image is a mapping from an image domain $\Omega \subset \mathbb{R}^2$ (here just a rectangle) to a range of values, e.g. real valued vectors of length three $\mathbb{R}^3$ for color images. Let $g$ be an image, i.e. a mapping as just described. Now, the famous piecewise-constant Mumford–Shah model approximates $g$ with an image that only has a fixed number $L$ of different color values. This is done by minimizing

$$E[(\mathcal{O}_l)_{l=1}^L, (c_l)_{l=1}^L] = \sum_{l=1}^{L} \left\{ \int_{\mathcal{O}_l} (g(x) - c_l)^2 \, \mathrm{d}x + \nu \operatorname{Per}(\mathcal{O}_l) \right\},$$

where $\mathcal{O}_1, \dots, \mathcal{O}_L$ is a partition of $\Omega$, e.g. the sets are pairwise disjoint and the union of their closures is equal to the closure of $\Omega$, i.e. $\bigcup_{j=1}^{n} \bar{\mathcal{O}}_j = \bar{\Omega}$, and, for $l = 1, \dots, L$, the vector $c_l \in \mathbb{R}^3$ is the

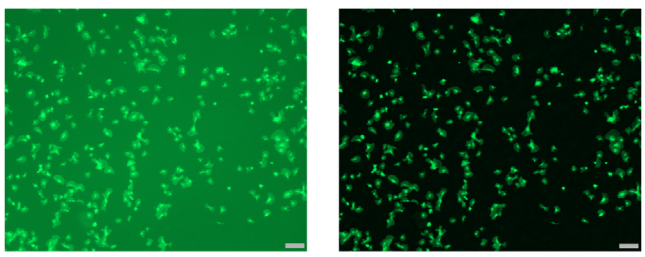

**Fig. 1.** A fluorescence image before (left) and after (right) background correction with the rolling ball algorithm; scale bar ≙ 20 µm (Clauser, 2019).

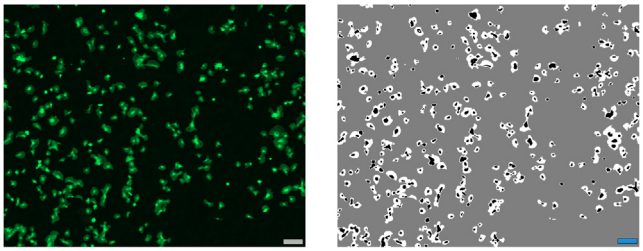

**Fig. 2.** A fluorescence image before (left) and after (right) image segmentation; scale bar ≙ 20 µm (Clauser, 2019). (For interpretation of the references to color in this figure legend, the reader is referred to the web version of this article.)

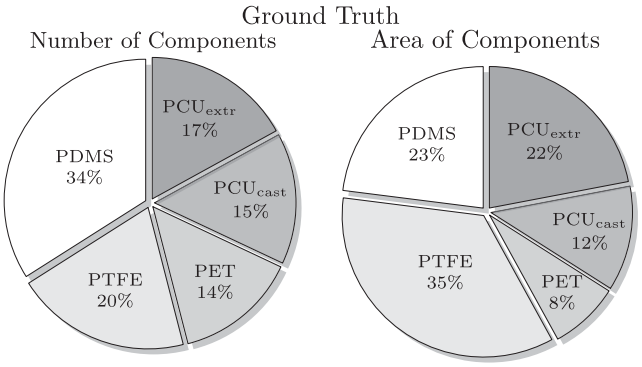


**Fig. 3.** Ground truth data distribution for the number of components (left) and the area of components (right).

mean color of $g$ in the segment $\mathcal{O}_l$. Per denotes the perimeter, i.e. the length of the boundary. Essentially, this means finding segments $\mathcal{O}_l$ and corresponding color values $c_l$, such that the color values of $g$ in a segment $\mathcal{O}_l$ are close to the color $c_l$, while trying to keep the boundary length of the sets $\mathcal{O}_l$ short. This latter is necessary to avoid very irregular segments and very small segments, which could be caused by noise in $g$. The corresponding minimization problem is non-convex and thus difficult to solve. We estimate the color values $c_l$ by $k$-means clustering of the color values of $g$ with $L$ clusters (MacQueen, 1967). As in Ref. Mevenkamp and Berkels (2016), we estimate the sets $\mathcal{O}_l$ using the convexification of the Mumford–Shah segmentation approach from Zach et al. (2008). The resulting convex optimization problem is solved with the primal–dual hybrid gradient method (Chambolle and Pock, 2011). We implemented the entire segmentation approach described above, including the initialization with $k$-means, in C++. Fig. 2 shows the result of the segmentation on the background corrected image from Fig. 1 with $L = 3$, i.e. when approximating the input image with three different color values.

One of the color values is used to approximate the black background, the other two are used to approximate the potential platelets with two different shades of green. This leads to a clear separation of the potential platelets from the background combined with a further separation of the potential platelets into brighter and darker areas, which are shown as black and white pixels in the right part of Fig. 2, respectively. Using connected components labeling on the non-background pixels (Shapiro, 1996), we extract the connected components of the result. Each of those is a potential platelet and needs to be classified as platelet or no platelet. For this, we derive a feature vector that contains the necessary information for the classification. The feature vector is computed for each component and consists of the total number of pixels (area) of the component, the number of brighter and darker image pixels in the component, the perimeter of the component and its circularity. The latter is defined as $\frac{P^2}{4\pi A}$, where $P$ is the perimeter and $A$ the area of the component. Additionally, the number of brighter and darker connected regions in each component and the ratio of bright to dark regions is computed for every component. These feature vectors are used as input for the following classification of each component since they represent specific platelet properties. The more activated a platelet is the larger it becomes, corresponding to a larger perimeter and a higher circularity. Ongoing activation also correlates with declining hyaloplasm, corresponding to bright regions with higher fluorescence intensity. Additionally, components with several separated bright regions enclosed into one large region with low intensity are likely to depict aggregates consisting of several platelets.

### 2.3. Random forest and prediction statistics

For the final analysis of the number and the area of adherent platelets on the microscopy images, a machine learning algorithm was set up. We used the implementation for the random forest algorithm from software package KNIME (KNIME AG, Switzerland). Training data for a supervised random forest (RF) model was obtained by manual classification of 19 628 components with an overall area of 7 257 484 px (0.0997 µm$^2$ px$^{-1}$).

These included 22 % 'no platelets', indicated as the positive class and accordingly 78 % 'platelets', the negative class. As the material the platelet adheres to impacts the platelet morphology, components from each material group were characterized. Note that aggregates formed by several platelets were considered as one component. Thus, the resulting area of components differs from the distribution of the number of components. Fig. 3 shows the distribution among the materials for both the number and the area of components.

The manually classified components were divided into training, validation and test data. In each subset, the above-mentioned ratio of positive and negative components was maintained. Table 2 shows the percentage of each data group for the number and the area of components.

The training data was used to set up a RF with specific parameters and the resulting RF was used to classify the validation data. Results were compared to the manual classification (ground truth) and prediction quality was evaluated by means of:

- accuracy (ACC)

$$ACC = \frac{TP + TN}{TP + FP + TN + FN} \tag{1}$$

**Table 1**
Materials for hemocompatibility testing.

| ID | Material | Manufacturer |
|---|---|---|
| M1 | PDMS: Poly(dimethylsiloxane) | Bess Medizintechnik GmbH, Germany |
| M2 | PTFE: Poly(tetrafluoro ethylene) | Bess Medizintechnik GmbH, Germany |
| M3 | PET: Poly(ethylene terephthalate) | ThermoFisher Scientific, USA |
| M4 | PCU$_{extr}$: Poly(carbonate urethane) – extrusion | Lubrizol, USA (raw material) |
| M5 | PCU$_{cast}$: Poly(carbonate urethane) – mold casting | Lubrizol, USA (raw material) |

- Mathews correlation coefficient (MCC)

$$MCC = \frac{TP \cdot TN - FP \cdot FN}{\sqrt{(TP+FP)(TP+FN)(TN+FP)(TN+FN)}} \tag{2}$$

- false positive rate (FPR)

$$FPR = \frac{FP}{TN+FP} = 1 - \text{specificity} \tag{3}$$

- false negative rate (FNR)

$$FNR = \frac{FN}{TP+FN} = 1 - \text{sensitivity} \tag{4}$$

$TP$: true positive; $TN$: true negative
$FP$: false positive; $FN$: false negative

This procedure was repeated adjusting the RF parameters until the maximum of prediction quality was reached. Adjustable parameters were split criterion, number of levels (tree depth), minimum node size and number of nodes. The following configuration achieved the best prediction outcome:

- split criterion: information gain ratio (NI)

$$NI = \frac{H(R) - \frac{|R_l|}{|R|}H(R_l) - \frac{|R_r|}{|R|}H(R_r)}{-\left(\frac{|R_l|}{|R|}\log_2\frac{|R_l|}{|R|} + \frac{|R_r|}{|R|}\log_2\frac{|R_r|}{|R|}\right)} \tag{5}$$

where $H$ denotes the Shannon entropy

$$H(R) = -\sum_{k=1}^{K} p_k \log_2 p_k \tag{6}$$

$p_k$: probability of $k$th class in $R$; $R_l$: population in left child node
$R$: total population; $R_r$: population in right child node

- number of levels: 100
- minimum node size: unconstrained
- number of nodes: unconstrained

Additionally to validation data prediction, a 10-fold cross validation was done to ensure independence of the model from the training data set. To this end, the union of training and validation data was randomly divided into 10 subsets of data, each with a positive/negative ratio of 21.45 %/78.55 %. A RF with the parameters described above was grown on 9 folds and validated against the ground truth on the remaining fold. This procedure was repeated 10 times, each time with another remaining validation fold.

Finally, the union of training and validation data was used to grow the final random forest. To evaluate the performance of the final RF, the so-far untouched test data set was predicted by this RF and the corresponding prediction statistics were computed. To further qualify the test data prediction, the Receiver–Operator-Characteristic (ROC) curve and the Precision–Recall (PR) curve, which are based on recall (7), fallout (8) and precision (9), were evaluated. The ROC curve represents recall vs fallout, whereas the PR curve depicts precision vs recall. The latter thereby takes an over-representation of the negative class more into account (Touw et al., 2013).

**Table 2**
Learning data sets for the random forest.

| Data set | Number of components/% | Area of components/% |
|---|---|---|
| Training data | 71.5 | 74.4 |
| Validation data | 17.9 | 18.5 |
| Test data | 10.6 | 7.1 |

**Table 3**
10-fold cross validation for the number and the area of components.

| | P/% | N/% | ACC | MCC | FPR/% | FNR/% |
|---|---|---|---|---|---|---|
| # Mean | 21.45 | 78.55 | 0.96 | 0.87 | 1.97 | 12.82 |
| # STD | ±0.02 | ±0.02 | ±0.01 | ±0.01 | ±0.45 | ±1.55 |
| A Mean | 7.23 | 92.77 | 0.96 | 0.70 | 0.62 | 41.11 |
| A STD | ±0.93 | ±0.93 | ±0.01 | ±0.07 | ±0.38 | ±9.23 |

$$\text{recall} = \text{sensitivity} = \frac{TP}{TP+FN} \tag{7}$$

$$\text{fallout} = FPR \tag{8}$$

$$\text{precision} = \frac{TP}{TP+FP} \tag{9}$$

### 2.4. Multi-person prediction

Supervised prediction models are subject to the risk of being biased by the person who has provided the learning data. The independence of the RF from the underlying data was verified in a multi-person prediction trial. Five people who were not involved in data collection before did a manual classification of a smaller subset of the ground truth data, including 1045 components with an area of 260 922 px. The distribution between positive (78 %) and negative (22 %) components was kept similar to the ground truth ratio. Prediction statistics were calculated for every pairwise combination of the seven available classifications, namely the RF, the original classifying person ('P1') and the five additional persons ('P2' to 'P6'). Note that the combination RF-P1 thus represents a part of the earlier calculated statistics during setting up the RF.

## 3. Results

This section first presents the random forest statistics for the algorithm itself, followed by the multi-person statistics. Finally, the newly developed, automated method is used to analyze the conducted in-vitro hemocompatibility experiment as a proof-of-concept.

The results of the 10-fold cross validation are shown in Table 3 for both the number (#) and the area (A) of components. The confusion matrix values are not shown as mean values and standard deviations are not reasonable for these numbers.

### 3.1. Random forest statistics

The distribution of positive (P) and negative (N) components is extremely imbalanced for the area of components as it was not specifically set. Nevertheless, values for ACC and MCC are in a similar high range for the number and the area of components. FPR is low for both cases with the higher value for the number of components with $1.97 \pm 0.45$. FNR is considerably higher, especially for the area of components ($41.11 \pm 9.23$). This means that about 40 % of the component area of positive components (no platelets) is characterized as the negative class (platelet). In general, all parameter show small standard deviations throughout the 10-fold cross validation.

Table 4 shows the prediction results of the test data by the final RF model for the number and the area of components. ACC and MCC are in a high range above 0.9 and 0.7, respectively, with slightly lower MCC for the area of components compared to the number of

**Table 4**
Test data prediction.

| | Number | Area/px |
|---|---|---|
| TP | 410 | 23 652 |
| FP | 83 | 5432 |
| TN | 1535 | 473 422 |
| FN | 55 | 11 451 |
| P/% | 22.32 | 6.83 |
| N/% | 77.68 | 93.17 |
| ACC | 0.93 | 0.97 |
| MCC | 0.81 | 0.72 |
| FPR/% | 5.13 | 1.13 |
| FNR/% | 11.83 | 32.62 |

components. The FPR for the number of components is with 5.13 % higher than for the area of components (1.13 %). By contrast, FNR is lower for the number of components (11.83 %), nevertheless, FNR for the area of components (32.62 %) is lower compared to the 10-fold cross validation. Note that the positive/negative component ratio is shifted again towards the negative class for the area of components.

Distinguishing the test data statistics with regard to the five different materials (cf. Supplementary Material, Table S1 & Table S2), the number of components shows only minor difference in prediction quality between all materials. ACC varies from 0.90 (PDMS) to 0.98 ($PCU_{extr}$) and MCC varies from 0.78 (PDMS) to 0.88 ($PCU_{extr}$), which is in accordance with the total statistics. PDMS reveals the highest FPR (5.39 %) and FNR (4.47 %). For the area of components, ACCs are slightly higher and MCCs are slightly lower compared to the number of components, which is in line with the previous results. FPRs are in general lower than for the number of components, whereas the FNR for PDMS (33.57 %) and PET (32.31 %) are in the high range of the total statistics.

To further quantify the prediction quality, the ROC curve and PR curve of the test data were calculated. The area under the ROC curve is 0.98 and the area under the PR curve is 0.85 for the number of components. For the area of components, results are similar with 0.94 and 0.77 for the area under the ROC and the PR curve, respectively. The graphs are provided in the supplementary (Fig. S1).

Detailed data for the multi-person prediction is shown in the supplementary material (Tables S3-S6). Comparing each classifier with each other shows only marginal differences and no tendencies. All ACCs are above 0.90 for both the number and the area of components, which is in line with all previous results. For some combinations, MCCs are slightly lower than the total RF statistics, however, the values are never lower than 0.62 (P5-RF). FPRs do not exceed 5 % for any combination, whereas FNRs range up to 24.05 % (P1-P4) for the number of components and 49.46 % (P5-RF) for the area of components.

### 3.2. Hemocompatibility analysis

The above developed and validated segmentation algorithm and the RF model were used to run a complete analysis of the hemocompatibility study. Fig. 4 shows the platelet covered surface area for the five different materials.

Cross bars indicate significant differences ($p < 0.05$), calculated by one-way analysis of variance for normally distributed data sets and Kruskal–Wallis test for non-normally distributed data, respectively (IBM SPSS Statistics 24, IBM, USA). PTFE shows the most covered surface area and the most scattered values with 18.75 % ± 9.50 %. Both PCU materials are in the range of 10% covered surface area and the least covered surface areas are found on PDMS and PET, both in the range of 1 %. Except of the combinations PDMS-PET and PTFE-$PCU_{extr}$, all differences between the materials are significant.

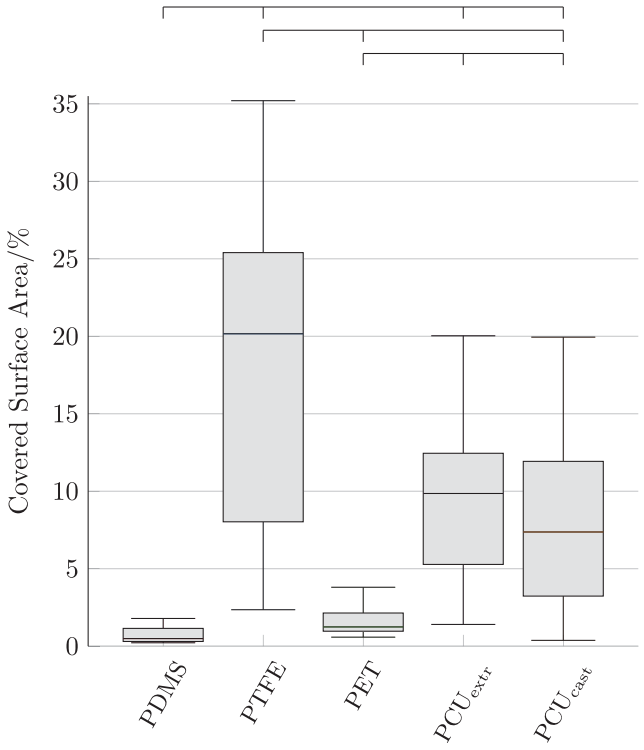


**Fig. 4.** Covered surface area, crossbar for $p < 0.05$ (Clauser, 2019).

## 4. Discussion

A new analysis method for in-vitro hemocompatibility tests was developed, including the automation of image segmentation and platelet analysis, using a RF algorithm. The individual steps of the procedure are depicted in Fig. 5. The scheme follows the common pipeline for cell segmentation and classification that is reported in the literature (Akram et al., 2016; Kan, 2017; Zinchuk and Grossenbacher-Zinchuk, 2020).

The quality of the image segmentation was evaluated by visual inspection, by comparing the original and the segmented version of different microscope images from each material group. The main criterion was the detailed depiction of platelet pseudopodia while maintaining the original platelet area. Although this is a manual interaction step, it has to be done only once during the set up of the algorithm and is thus acceptable. Continuous control of images throughout the whole study proved the segmentation to be precise for a large number of diverse images (> 200); thus a possible error based on the manual interaction is negligible. Although open source platforms such as ilastik, CellProfiler, xgboost, offer a number of microscopy segmentation algorithms, none provides a solution for the specific application of the current study (Carpenter et al., 2006; Berg et al., 2019). Therefore, our custom approach tailored to platelet segmentation was essential for the success of the study.

The RF for platelet characterization was set up in a supervised manner. To avoid the bias of manual image selection, images were chosen randomly from all five material groups. The large number of classified components (nearly 20 000) ensures a good representation of all data by the ground truth. As PDMS turned out to be the most critical material in terms of protein residues, more components were classified from this material group. For the evaluation of a material's hemocompatibility, the area covered with platelets is a crucial parameter. Thus, not only the number but also the area of components is evaluated by the RF. The area of 'one' component can differ immensely depending on the type of component. A single platelet covers an area of around 10 $\mu m^2$ whereas

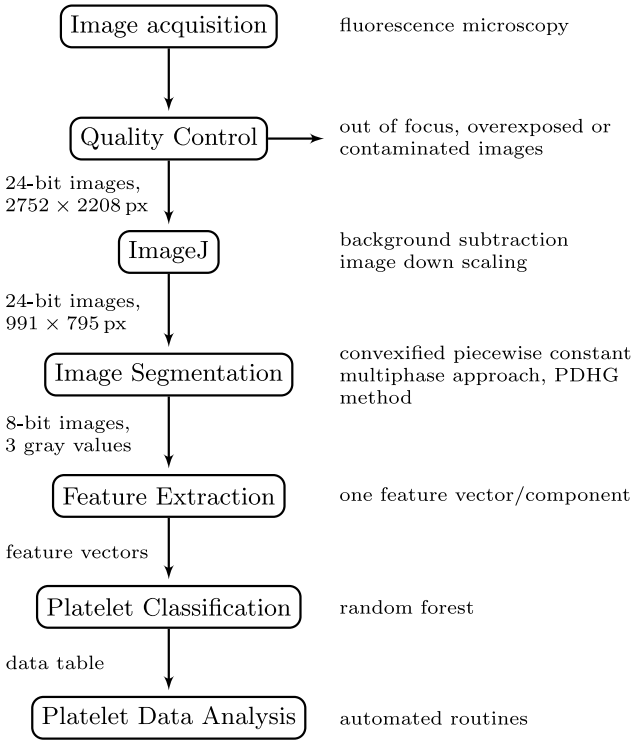


**Fig. 5.** Scheme of the automated analysis method.

a platelet aggregate consisting of numerous connected platelets could cover a whole microscope image. Accordingly, positive–negative class ratios are shifted towards the negative class as the distribution was set for the number of components. This is the reason why prediction values that take the positive class underrepresented here-in more into consideration are slightly lower for the area of components than for the number of components. Nevertheless, all prediction statistics reveal ACC and MCC to be considerably above 0.5 and 0, respectively, which is the threshold indicating a well-founded prediction rather than a random choice. This outcome is supported by the areas under the ROC and the PR curve, which are all close to 1.

RF statistics cannot directly be compared to similar studies as there are only very few reported approaches that deal with cell or particularly blood cell characterization. Nevertheless, some groups aimed at machine learning-based classification using different classifiers that will be discussed in the following. Razzak et al. made use of contour aware segmentation to isolate red and white blood cells (RBCs and WBCs, respectively) from microscopic blood smears. Further on, they used CNN classification to distinguish both cell types into subgroups, namely the five different classes of WBCs and five unphysiological shapes of deformed RBCs (Razzak and Naz, 2017). With a data set of 64 000 cells in total, the RBC/WBC segmentation achieved a high accuracy of 98 %, whereas the cell differentiation reached an accuracy of 87.47 % to 93.69 % for RBCs and 90.00 % to 98.80 % for WBCs. Ferdosi et al. and Zhang et al. aimed at WBC classification as well. Working with a ground truth of 250 images (720 × 576 px), Ferdosi et al. utilized $k$-means clustering and morphological operators to segment WBCs from fluorescence microscopy images. Best classification results were achieved for the WBC class of Basophils with a precision of 98.36 % and a sensitivity of 96.49 % (Ferdosi et al., 2018). Similar results were presented by Zhang et al. who achieved an accuracy of 98 % and 92 % for segmentation and classification, respectively. Thereby, 1350 images (1600 × 1200 px) with a maximum of 5 cells per image were segmented using a feature extraction process and further classified using a support vector machine (Zhang et al., 2020). For the purpose of sickle cell diagnostics, Xu et al. and Zhang et al. dealt with RBC classification more detailed. On the basis of 7206 single RBCs that were imaged microscopically after pre-sorting by means of density fractionated labeling, RBCs were segmented and separated in case of overlapping and finally classified with a deep CNN into 5 and 8 classes, respectively (Xu et al., 2017). Accuracy and AUC resulted to 89.28 % and 0.97 for 5 classes and 87.5 % and 0.94, respectively. An improvement in accuracy was achieved by Zhang et al. who implemented a deformable U-Net. With 166 training images (1920 × 1080 px), three different classes of RBCs could be predicted with an accuracy of 99 % (Zhang et al., 2018). Comparing all these prediction scores to our RF statistics, our results are located in the upper range with accuracies of 93 % and 97 %, respectively, and are thus comparable to other blood cell classification approaches. In contrast to the presented studies, we had to use a considerably larger database of 20 000 ground truth components to achieve this high prediction accuracy. This highlights the challenge of platelet segmentation and characterization due to the enormous variety and complexity of morphological shapes of single platelets and platelet aggregates. A recent study by Pike et al. addresses this issue in a semi-automated manner. The user first has to manually mark every platelet, afterwards each individual platelet is separated and classified according to its activation state with a random forest. Build upon a training data set of 1732 single platelets, 90 % prediction accuracy was achieved (Pike et al., 2020). In contrast to our study, a differentiation between platelet and other blood components, i.e. RBCs, WBCs, proteins, was not required as the scope of Pike et al. was a microscopical platelet function analysis of washed platelets. For the purpose of hemocompatibility test analysis, which is the case in our study, this differentiation between platelets and other blood components is essential for the usability of the analysis method. Furthermore, a manual marking of individual platelets is not feasible in our case due to the enormous number of platelets that need to be classified (≫ 200 000).

Having a more detailed look at our RF error rates, considerably higher FNRs than FPRs are observed. This means, a certain amount of 'no platelets' are characterized as platelets. In the context of material thrombogenicity assessment, this represents a worst-case-scenario in terms of hemocompatibility rating. Although the aim is the most perfect characterization as possible, however, a slight overrating in terms of thrombogenicity can be considered as an additional level of safety. The underestimation of a material's thrombogenicity can have a severe and even life-threatening impact on patients, thus, realistic predictions are crucial. For FPRs, values are in the range of 5 % or lower, which represents a very small error rate for platelets characterized as no platelets. Interestingly, other studies that reported the sensitivity as the counterpart of FPR and the specificity as the counterpart of FNR present a similar phenomenon (Gray et al., 2013; Li et al., 2012; Liu et al., 2010; Wu et al., 2009). Possibly, high FNRs can be attributed to the field of biomedical imaging, where the over-represented negative class contains characteristic components, whereas the positive class can appear in a variety of components such as imaging artifacts or cell residues.

In order to evaluate whether the established random forest was overfitted to the training data set, a 10-fold cross validation was carried out. Throughout all 10 folds, results were very similar, resulting in low standard deviations. This indicates the RF model to be independent from the underlying training data and suitable for the classification of unknown and new data.

Furthermore, the prediction quality was studied separately for all five materials. Since various materials affect platelets differently, shape and size of adherent platelets varies from material to material. Within the manually classified ground truth data set, components from all material groups were included. Nevertheless, we needed to rule out that our proposed method predicts platelets on some materials better than on others. In general, ACCs, MCCs and FPRs are in a similar range for all five materials. Some outliers are present in the MCC for the area of components with values down to 0.51 ($PCU_{cast}$). This drop of

MCC can be explained by the extremely low fraction ($< 1\,\%$) of the positive class for this material and is not due to a RF weakness. The only material-related effects are observed for FNRs. Whereas differences between materials are small for the number of components, the area of components shows strong differences for some materials. PDMS and PET show FNRs in the range of the total FNR, contrarily, the other three materials result in considerably lower FNRs. On the one hand, this is in line with the optical impression that PDMS presents the highest number of difficult to classify positive components (e.g. proteins). On the other hand, the results are in contrast to the general finding that FNRs increase with decreasing portions of positive components. In conclusion, the proposed method predicts platelets on different materials well with the limitation that an elevated number of uncharacteristic positive components results in higher FNRs. This can be overcome in the future by either improving the quality of images and thus reducing the appearance of such components or by including more of these specific components into the ground truth of the random forest training data set.

A general source of error is the supervised setup, which might be biased by the manual classification of a single person. The multi-person comparison shows that the RF developed within this study is not noticeably biased in this regard. Within the different person–person and person–RF combinations there were no differences either for the number or the area of components in terms of ACC, MCC and error rates. Of course, some combinations showed slightly better results than others, but there was no clear pattern for any combination being superior to all others. Error rates are generally lower compared to the final RF values, this is probably due to the smaller data subset with only about 1000 components and consequently less variability within this subset.

Finally, the whole hemocompatibility study was analyzed by means of the newly developed automatized analysis method, which combines image segmentation and a RF. The results are generally in line with the expectations, since materials with a known outcome were tested (Braune et al., 2017). PTFE shows the most platelet adhesion and activation as the platelet covered area is significantly higher compared to all other materials (Braune et al., 2017; Chandy et al., 2000; Freeman et al., 2018). PDMS shows a very low platelet adhesion affinity, which corresponds to its reported good short-term hemocompatibility (Spiller et al., 2007; Khorasani and Mirzadeh, 2004). The remaining materials are situated in between this range as expected (Chandy et al., 2000; Clauser et al., 2014). In contrast to a previous study, no significant differences were observed for PET compared to PDMS (Braune et al., 2017). This might be due to the new analysis technique that allows for analyzing the whole material sample area. Without automation of platelet counting and characterization, only small fractions of the material sample can be analyzed, which might lead to varying results.

Overall, all statistics and results give evidence that the established RF in combination with the segmentation algorithm is a suitable tool for the automated classification of platelets on fluorescence microscopy images. However, a RF is always tailored to a specific problem due to the underlying ground truth data used for training. Therefore, the transferability to other microscopy techniques (e.g. Scanning Electron Microscopy, Laserscanning Microscopy), staining methods (e.g. specific P-selectin staining) and materials has to be evaluated before the RF can be applied to those images. Only if the appearance of platelets is the same in terms of size, stained area, resolution, etc., the RF can be applied without the need for a new training based on the new ground truth. This restriction applies also for the segmentation algorithm. If, for example, the image quality, resolution or platelet appearance differs severely to the here-in used images, segmentation might become imprecise. In this case, segmentation parameters have to be adjusted to the present case. Nonetheless, every segmentation and classification algorithm faces this problem which is therefore a global restriction and not an explicit shortcoming of our developed method.

In general, more information and additional features could be extracted from the segmentation results, which might improve the quality of platelet characterization. For instance, one could consider additional elementary shape features like convexity (ratio of the perimeter of the convex hull and the perimeter), solidity (ratio of the area and the area of the convex hull) or even full shape descriptors designed for closed contours like curvature-based Fourier shape descriptors (El-ghazal et al., 2012).

A further improvement of the developed automated platelet analysis would overcome the manual image inspection prior to the image segmentation. This could be achieved by an additional pre-processing step prior to platelet classification. As an example, a convolutional neural network could be used for the first image sorting since it is capable for large data-set classification (Castilla et al., 2018; Pang et al., 2017). Furthermore, a more distinct platelet characterization with regard to the activation state of the platelets would reveal more details of the material–blood interaction.

Although there is room for improvements, the developed analysis method is the first approach for an automatized platelet analysis for hemocompatibility evaluation. Thus, it offers the possibility for fast and reproducible in-vitro experiment analyses in the future. This is a first and important step towards the standardization of biomaterial hemocompatibility evaluations, which will contribute to further progress in the development of blood-contacting medical devices.

## 5. Conclusion

In this study, we developed and validated a new tool for the analysis of platelet adhesion on biomaterials after in-vitro testing. The novel method includes automatized image segmentation and platelet characterization by means of a Mumford–Shah model and a random forest, respectively. The methods allows overcoming the limitations of (semi-)manual platelet count techniques used so far. Particularly, a user-independent accuracy in platelet prediction of $> 90\,\%$ was achieved while time effort was remarkably reduced. Furthermore, this automatized platelet analysis approach presents a unique method for comparable and reproducible hemocompatibility investigation in the future and thus serves as the first step towards the standardization of biomaterial hemocompatibility evaluation.

## CRediT authorship contribution statement

**Johanna C. Clauser:** Conceptualization, Formal analysis, Validation, Writing - original draft, Visualization. **Judith Maas:** Investigation. **Jutta Arens:** Project administration, Writing - review & editing. **Thomas Schmitz-Rode:** Writing - review & editing. **Ulrich Steinseifer:** Supervision. **Benjamin Berkels:** Software, Formal analysis, Writing - original draft.

## Declaration of competing interest

The authors declare that they have no known competing financial interests or personal relationships that could have appeared to influence the work reported in this paper.

## Acknowledgments

The authors like to thank Dr. Doris Keller from the University Medical Center RWTH Aachen University for the blood withdrawal and Leyla Haferkamp from the RWTH Aachen University Language Center for proof reading.

Calculations were performed with computing resources granted by RWTH Aachen University under project rwth0314. The authors have no competing interests to declare.

This study was partly funded by the INTERREG Program V-A Euregio Maas-Rhine of the European Union (Grant Number 2016/98602).

B. Berkels was funded in part by the Excellence Initiative of the German Federal and State Governments through grant GSC 111.

This article comprises results and figures that a part of the PhD Thesis from Johanna C. Clauser, submitted at RWTH Aachen University, Germany, in 2019 (Clauser, 2019).

## Appendix A. Supplementary data

Supplementary material related to this article can be found online at https://doi.org/10.1016/j.engappai.2020.104009.

## References


Akram, S.U., Kannala, J., Eklund, L., Heikkilä, J., 2016. Cell segmentation proposal network for microscopy image analysis. In: Carneiro, G., Mateus, D., Peter, L., Bradley, A., Tavares, J.M.R.S., Belagiannis, V., Papa, J.P., Nascimento, J.C., Loog, M., Lu, Z., Cardoso, J.S., Cornebise, J. (Eds.), Deep Learning and Data Labeling for Medical Applications. In: Lecture Notes in Computer Science, vol. 10008, Springer International Publishing, Cham and s.l., pp. 21–29. http://dx.doi.org/10.1007/978-3-319-46976-8_3.

Altan, A., Karasu, S., 2020. Recognition of COVID-19 disease from X-ray images by hybrid model consisting of 2D curvelet transform, chaotic salp swarm algorithm and deep learning technique. Chaos Solitons Fractals 140, 110071. http://dx.doi.org/10.1016/j.chaos.2020.110071.

Berg, S., Kutra, D., Kroeger, T., Straehle, C.N., Kausler, B.X., Haubold, C., Schiegg, M., Ales, J., Beier, T., Rudy, M., Eren, K., Cervantes, J.I., Xu, B., Beuttenmueller, F., Wolny, A., Zhang, C., Koethe, U., Hamprecht, F.A., Kreshuk, A., 2019. Ilastik: interactive machine learning for (bio)image analysis. Nat. Methods 16 (12), 1226–1232. http://dx.doi.org/10.1038/s41592-019-0582-9.

Braune, S., Gros, M., Walter, M., Zhou, S., Dietze, S., Rutschow, S., Lendlein, A., Tschoepe, C., Jung, F., 2016. Adhesion and activation of platelets from subjects with coronary artery disease and apparently healthy individuals on biomaterials. J. Biomed. Mater. Res. Part B 104 (1), 210–217.

Braune, S., Grunze, M., Straub, A., Jung, F., 2013. Are there sufficient standards for the in vitro hemocompatibility testing of biomaterials?. Biointerphases 8 (1), 33.

Braune, S., Sperling, C., Maitz, M.F., Steinseifer, U., Clauser, J., Hiebl, B., Krajewski, S., Wendel, H.P., Jung, F., 2017. Evaluation of platelet adhesion and activation on polymers: Round-robin study to assess inter-center variability. Colloids Surfaces B 158, 416–422.

Carpenter, A.E., Jones, T.R., Lamprecht, M.R., Clarke, C., Kang, I.H., Friman, O., Guertin, D.A., Chang, J.H., Lindquist, R.A., Moffat, J., Golland, P., Sabatini, D.M., 2006. Cellprofiler: image analysis software for identifying and quantifying cell phenotypes. Genome Biol. 7 (10), R100. http://dx.doi.org/10.1186/gb-2006-7-10-r100.

Castilla, C., Maska, M., Sorokin, D.V., Meijering, E., Ortiz-de Solorzano, C., 2018. Segmentation of actin-stained 3D fluorescent cells with filopodial protrusions using convolutional neural networks. In: 2018 IEEE 15th International Symposium on Biomedical Imaging (ISBI 2018). IEEE, Piscataway, NJ, pp. 413–417.

Chambolle, A., Pock, T., 2011. A first-order primal-dual algorithm for convex problems with applications to imaging. J. Math. Imaging Vis. 40 (1), 120–145. http://dx.doi.org/10.1007/s10851-010-0251-1.

Chandy, T., Das, G.S., Wilson, R.F., Rao, G.H., 2000. Use of plasma glow for surface-engineering biomolecules to enhance bloodcompatibility of dacron and PTFE vascular prosthesis. Biomaterials 21 (7), 699–712.

Clauser, J.C., 2019. A New Analysis Method for Optical in-Vitro Hemocompatibility Assessment. (Dissertation). Shaker Verlag Dueren, Germany.

Clauser, J., Gester, K., Roggenkamp, J., Mager, I., Maas, J., Jansen, S.V., Steinseifer, U., 2014. Micro-structuring of polycarbonate-urethane surfaces in order to reduce platelet activation and adhesion. J. Biomater. Sci., Polym Ed. 25 (5), 504–518.

DIN ISO 10993-4:2017, 2017. Biological evaluation of medical devices - part 4: Selection of tests for interactions with blood.

El-ghazal, A., O., B., Belkasim, S., 2012. Invariant curvature-based fourier shape descriptors. J. Vis. Commun. Image Represent. 23 (4), 622–633. http://dx.doi.org/10.1016/j.jvcir.2012.01.011.

Ferdosi, B.J., Nowshin, S., Sabera, F.A., Habiba, 2018. White blood cell detection and segmentation from fluorescent images with an improved algorithm using k-means clustering and morphological operators. In: 4th International Conference on Electrical Engineering and Information & Communication Technology. pp. 566–570. http://dx.doi.org/10.1109/CEEICT.2018.8628068.

Ferreira, T., Rasband, W., 2012. ImageJ User Guide: IJ 1.46r. National Institutes of Health, Bethesda, USA.

Freeman, J., Chen, A., Weinberg, R.J., Okada, T., Chen, C., Lin, P.H., 2018. Sustained thromboresistant bioactivity with reduced intimal hyperplasia of heparin-bonded polytetrafluoroethylene propaten graft in a chronic canine femoral artery bypass model. Ann. Vasc. Surg. 49, 295–303.

Fuyong, X., Yuanpu, X., Hai, S., Fujun, L., Lin, Y., 2018. Deep learning in microscopy image analysis: A survey. IEEE Trans. Neural Netw. Learn. Syst. 29 (10), 4550–4568. http://dx.doi.org/10.1109/TNNLS.2017.2766168.

Gray, K.R., Aljabar, P., Heckemann, R.A., Hammers, A., Rueckert, D., 2013. Random forest-based similarity measures for multi-modal classification of Alzheimer's disease. NeuroImage 65, 167–175.

Jaffer, I.H., Fredenburgh, J.C., Hirsh, J., Weitz, J.I., 2015. Medical device-induced thrombosis: What causes it and how can we prevent it? J. Thromb. Haemost. 13, 72–81.

Kan, A., 2017. Machine learning applications in cell image analysis. Immunol. Cell Biol. 95 (6), 525–530. http://dx.doi.org/10.1038/icb.2017.16.

Khan, A.O., Maclachlan, A., Lowe, G.C., Nicolson, P.L.R., Ghaithi, R.A., Thomas, S.G., Watson, S.P., Pike, J.A., Morgan, N.V., 2020. High-throughput platelet spreading analysis: a tool for the diagnosis of platelet-based bleeding disorders. Haematologica 105 (3), e124–e128. http://dx.doi.org/10.3324/haematol.2019.225912.

Khorasani, M.T., Mirzadeh, H., 2004. In vitro blood compatibility of modified PDMS surfaces as superhydrophobic and superhydrophilic materials. J. Appl. Polym. Sci. 91 (3), 2042–2047.

Li, B.-Q., Feng, K.-Y., Chen, L., Huang, T., Cai, Y.-D., 2012. Prediction of protein-protein interaction sites by random forest algorithm with mRMR and IFS. PloS One 7 (8), e43927.

Liu, Z.-P., Wu, L.-Y., Wang, Y., Zhang, X.-S., Chen, L., 2010. Prediction of protein-RNA binding sites by a random forest method with combined features. Bioinformatics 26 (13), 1616–1622.

Lutter, C., Nothhaft, M., Rzany, A., Garlichs, C.D., Cicha, I., 2015. Effect of specific surface microstructures on substrate endothelialisation and thrombogenicity: Importance for stent design. Clin. Hemorheol. microcirc. 59 (3), 219–233.

MacQueen, J., 1967. Some methods for classification and analysis of multivariate observations. In: Proceedings of the Fifth Berkeley Symposium on Mathematical Statistics and Probability, Volume 1: Statistics. University of California Press, Berkeley, Calif., pp. 281–297.

Mevenkamp, N., Berkels, B., 2016. Variational multi-phase segmentation using high-dimensional local features. In: IEEE Winter Conference on Applications of Computer Vision (WACV 2016). IEEE, arXiv:1902.09863.

Mumford, D., Shah, J., 1989. Optimal approximations by piecewise smooth functions and associated variational problems. Comm. Pure Appl. Math. 42 (5), 577–685. http://dx.doi.org/10.1002/cpa.3160420503.

Nadzeyka, I., Bolle, E., Moos, M., Kunitz, P., Steinseifer, U., Schmitz-Rode, T., 2017. Process analysis of spray atomization of dissolved polymers for manufacturing of blood-compatible textile implants. J. Ind. Text. 48 (5), 926–940.

Pang, S., Yu, Z., Orgun, M.A., 2017. A novel end-to-end classifier using domain transferred deep convolutional neural networks for biomedical images. Comput. Methods Programs Biomed. 140, 283–293.

Pereira, S., Meier, R., McKinley, R., Wiest, R., Alves, V., Silva, C.A., Reyes, M., 2018. Enhancing interpretability of automatically extracted machine learning features: application to a RBM-random forest system on brain lesion segmentation. Med. Image Anal. 44, 228–244. http://dx.doi.org/10.1016/j.media.2017.12.009.

Pham, T.T., Wiedemeier, S., Maenz, S., Gastrock, G., Settmacher, U., Zanow, J., K.D., J., Lüdecke, C., Joensson, J.B., 2016. Hemodynamic aspects of reduced platelet adhesion on bioinspired microstructured surfaces. Colloids Surfaces B 145, 502–509.

Pike, J.A., Simms, V.A., Smith, C.W., Morgan, N.V., Khan, A.O., Poulter, N.S., Styles, I.B., Thomas, S.G., 2020. An adaptable analysis workflow for characterization of platelet spreading and morphology. Platelets 1–5. http://dx.doi.org/10.1080/09537104.2020.1748588.

Ratner, B.D., 2007. The catastrophe revisited: Blood compatibility in the 21st century. Biomaterials 28 (34), 5144–5147.

Ratner, B.D., Hoffman, A.S., Schoen, F.J., Lemons, J.E. (Eds.), 2013. Biomaterials Science: An Introduction to Materials in Medicine, third ed. Academic, Cambridge, USA.

Razzak, M.I., Naz, S., 2017. Microscopic blood smear segmentation and classification using deep contour aware CNN and extreme machine learning. In: CVPRW 2017. IEEE, Piscataway, NJ, pp. 801–807. http://dx.doi.org/10.1109/CVPRW.2017.111.

Sefton, M.V., Sawyer, A., Gorbet, M., Black, J.P., Cheng, E., Gemmell, C., Pottinger-Cooper, E., 2001. Does surface chemistry affect thrombogenicity of surface modified polymers?. J. Biomed. Mater. Res. 55 (4), 447–459.

Shapiro, L.G., 1996. Connected component labeling and adjacency graph construction. In: Kong, T.Y., Rosenfeld, A. (Eds.), Topological Algorithms for Digital Image Processing. In: Machine Intelligence and Pattern Recognition, vol. 19, North-Holland, pp. 1–30. http://dx.doi.org/10.1016/S0923-0459(96)80011-5.

Sheth, S.A., Lopez-Rivera, V., Barman, A., Grotta, J.C., Yoo, A.J., Lee, S., Inam, M.E., Savitz, S.I., Giancardo, L., 2019. Machine learning-enabled automated determination of acute ischemic core from computed tomography angiography. Stroke 50 (11), 3093–3100. http://dx.doi.org/10.1161/STROKEAHA.119.026189.

Spiller, D., Losi, P., Briganti, E., Sbrana, S., Kull, S., Martinelli, I., Soldani, G., 2007. PDMS content affects in vitro hemocompatibility of synthetic vascular grafts. J. Mater. Sci.: Mater. Med. 18 (6), 1097–1104. http://dx.doi.org/10.1007/s10856-006-0067-0.

Touw, W.G., Bayjanov, J.R., Overmars, L., Backus, L., Boekhorst, J., Wels, M., van Hijum, S.A., 2013. Data mining in the life sciences with random forest: a walk in the park or lost in the jungle? Brief. Bioinform. 14 (3), 315–326.

Vantaram, S.R., Saber, E., 2012. Survey of contemporary trends in color image segmentation. J. Electron. Imaging 21 (4), 040901–1–040901–28. http://dx.doi.org/10.1117/1.JEI.21.4.040901.

Wu, J., Liu, H., Duan, X., Ding, Y., Wu, H., Bai, Y., Sun, X., 2009. Prediction of DNA-binding residues in proteins from amino acid sequences using a random forest model with a hybrid feature. Bioinformatics 25 (1), 30–35.

Xu, M., Papageorgiou, D.P., Abidi, S.Z., Dao, M., Zhao, H., Karniadakis, G.E., 2017. A deep convolutional neural network for classification of red blood cells in sickle cell anemia. PLoS Comput. Biol. 13 (10), e1005746. http://dx.doi.org/10.1371/journal.pcbi.1005746.

Zach, C., Gallup, D., Frahm, J.-M., Niethammer, M., 2008. Fast global labeling for real-time stereo using multiple plane sweeps. In: VMV. pp. 243–252.

Zhang, M., Li, X., Xu, M., Li, Q., 2018. RBC semantic segmentation for sickle cell disease based on deformable u-net. In: Frangi, A.F., Schnabel, J.A., Davatzikos, C., Alberola-López, C., Fichtinger, G. (Eds.), Medical Image Computing and Computer Assisted Intervention – MICCAI 2018. In: Lecture Notes in Computer Science, vol. 11073, Springer, Cham, pp. 695–702. http://dx.doi.org/10.1007/978-3-030-00937-3_79.

Zhang, Y., Xu, N., Chen, H., Lam, W.H., Zhang, X., Qiu, T., 2020. A robust and high-performance white blood cell segmentation algorithm. In: 2020 5th International Conference on Computer and Communication Systems (ICCCS). IEEE, pp. 347–351. http://dx.doi.org/10.1109/ICCCS49078.2020.9118569.

Zhou, M., Yang, J., Ye, X., Zheng, A., Li, G., Yang, P., Zhu, Y., Cai, L., 2008. Blood platelet's behavior on nanostructured superhydrophobic surface. J. Nano Res. 2, 129–136.

Zinchuk, V., Grossenbacher-Zinchuk, O., 2020. Machine learning for analysis of microscopy images: A practical guide. Curr. Protoc. Cell Biol. 86 (1), e101. http://dx.doi.org/10.1002/cpcb.101.